eScience

Controlled synthesis of MOF-derived hollow and yolk–shell nanocages for improved water oxidation and selective ethylene glycol reformation

Minghong Huang[1,2,3], Changsheng Cao[2], Li Liu[2], Wenbo Wei[2], Qi-Long Zhu[2,3,*], Zhenguo Huang[1,*]

[1] *School of Civil & Environmental Engineering, University of Technology Sydney, Ultimo, New South Wales 2007, Australia*

[2] *State Key Laboratory of Structural Chemistry, Fujian Institute of Research on the Structure of Matter, Chinese Academy of Sciences (CAS), Fuzhou 350002, China*

[3] *Fujian Science & Technology Innovation Laboratory for Optoelectronic Information of China, Fuzhou 350108, China*

[*]Corresponding author.

E-mail: zhenguo.huang@uts.edu.au (Z. Huang); qlzhu@fjirsm.ac.cn (Q. Zhu).

Abstract

Delicately designed metal–organic framework (MOF)-derived nanostructured electrocatalysts are essential for improving the reaction kinetics of the oxygen evolution reaction and tuning the selectivity of small organic molecule oxidation reactions. Herein, novel oxalate-modified hollow CoFe-based layered double hydroxide nanocages (h-CoFe-LDH NCs) and yolk–shell ZIF@CoFe-LDH nanocages (ys-ZIF@CoFe-LDH NCs) are developed through an etching–doping reconstruction strategy from a Co-based MOF precursor (ZIF-67). The distinctive nanostructures, along with the incorporation of the secondary metal element and intercalated oxalate groups, enable h-CoFe-LDH NCs and ys-ZIF@CoFe-LDH NCs to expose more active sites with high intrinsic activity. The resultant h-CoFe-LDH NCs exhibit outstanding OER activity with an overpotential of only 278 mV to deliver a current density of 50 mA cm^{-2}. Additionally, controlling the reconstruction degree enables the formation of ys-ZIF@CoFe-LDH NCs with a yolk–shell nanocage nanostructure, which show outstanding electrocatalytic performance for the selective ethylene glycol oxidation reaction (EGOR) toward formate, with a Faradaic efficiency of up to 91%. Consequently, a hybrid water electrolysis system integrating the EGOR and the hydrogen evolution reaction using Pt/C||ys-ZIF@CoFe-LDH NCs is explored for energy-saving hydrogen production, requiring a cell voltage 127 mV lower than water electrolysis to achieve a current density of 50 mA cm^{-2}. This work demonstrates a feasible way to design advanced MOF-derived electrocatalysts toward enhanced electrocatalytic reactions.

Keywords: Metal–organic frameworks; LDH nanocages; Yolk–shell structure; Oxygen evolution; Ethylene glycol oxidation

1. Introduction

Structural engineering is regarded as an effective path to improve the electrochemical performance of electrode materials [1]. Hollow and yolk–shell nanostructures have demonstrated advantages as functional materials for electrocatalysis owing to their unique configurations and inherent physical and chemical properties, such as large surface areas, rich cavities, low mass density, and reduced diffusion distances for mass and charge transport [2, 3]. Yolk–shell nanostructures in particular possess hollow shells and interior cores featuring multiple structural merits that make them incredibly attractive for electrocatalysis. As a result, numerous synthetic strategies have been developed to fabricate hollow frame-like and yolk–shell nanoarchitectures based on various precursors [4-7]. For instance, the most efficient approach for preparing such nanostructures is the template-assisted method, in which sacrificial templates can be transformed into various target products through careful etching and/or pyrolysis [8, 9]. Because metal−organic frameworks have accessible porous crystalline structures that enable high mass transport, they often serve as the starting sacrificial templates for synthesizing high-performance hollow and yolk–shell nanostructured electrocatalysts [10]. Most pristine MOFs cannot be used in practical energy conversion and storage applications because of their intrinsically low electrical conductivity and poor structural stability [11, 12]. This limitation can be overcome through converting MOFs to diverse derivatives (e.g., layered double hydroxides (LDHs), carbonaceous materials, metal oxides, and metal sulfides) that have more beneficial properties and nanostructures while retaining high porosities [13-15].

MOF-derived LDHs, particularly Co-LDHs, have proven to be efficient electrocatalysts for the oxygen evolution reaction (OER) [16, 17]. However, the performance is still far from satisfactory for practical water electrolysis, due to poor intrinsic activity and insufficient active sites [18]. Previous studies have shown that the introduction of foreign metal atoms into Co-LDHs can enhance the OER performance, since the synergistic interactions between Co and foreign metals can tune the local coordination environment and electronic structure of Co sites, thereby boosting the intrinsic activity [19-23]. For example, Wang's research group reported that incorporating Zn^{2+} ions into CoOOH can give rise to oxygen non-bonding states with different local configurations and change the OER routes. $Zn_{0.2}Co_{0.8}OOH$ with a Zn–O2–Co–O2–Zn configuration showed much better catalytic activity than the corresponding monometallic component [23]. However, obtaining MOF-derived hollow and yolk–shell LDH catalysts with optimized compositions is still challenging due to complex synthetic procedures and differences between the precipitation kinetics of divalent and trivalent metal cations [24].

It is well known that the sluggish kinetics of the anodic OER make it a bottleneck reaction in water electrolysis [25, 26]. Therefore, the OER is an energy-intensive process and only produces a low-value product (i.e., O_2). Alternatively, replacing the OER with thermodynamically favorable small organic molecule oxidation reactions is attractive to reduce energy input while simultaneously producing value-added products, as verified by previous studies [27-32]. Notably, Co-based LDH electrocatalysts have shown high activity for the electro-reforming of some organic fuels. For example, with cobalt hydroxide@hydroxysulfide nanosheets on carbon paper ($Co(OH)_2$@HOS/CP) as the working electrode, methanol can be selectively converted into formate with a Faradaic efficiency (FE) as high as ~100% [33]. Replacing the OER with the methanol oxidation reaction (MOR) in a hybrid water electrolysis system enables the simultaneous production of H_2 and formate with less energy input. In light of these encouraging findings, it is desirable to construct MOF-derived Co-based LDHs with delicately controlled compositions and morphologies as bifunctional electrocatalysts for water oxidation and selective ethylene glycol (EG) reformation for enhanced H_2 production.

Herein, an etching-doping reconstruction strategy was developed to synthesize oxalate-decorated hierarchical nanostructured CoFe-LDHs by using a Co-based MOF (ZIF-67) as the precursor. Through deliberately adjusting the reconstruction degree under various conditions, hollow CoFe-LDH nanosheets (NSs) assembled into nanocages (h-CoFe-LDH NCs) and yolk–shell ZIF@CoFe-LDH nanocages (ys-

ZIF@CoFe-LDH NCs) were readily synthesized. Control experiments revealed that the strong affinity between oxalate groups and Co^{2+}/Fe^{3+} ions is the key to the formation of the unique hierarchical nanostructures. Owing to the strong synergistic interactions between Co and Fe sites, as well as enlargement of the LDH layer spacing by the oxalate groups, the as-prepared h-CoFe-LDH NCs and ys-ZIF@CoFe-LDH NCs exhibited excellent electrochemical performance for the OER and the ethylene glycol oxidation reaction (EGOR), respectively. Assembling ys-ZIF@CoFe-LDH NCs as the anode in an EGOR-coupled hybrid water electrolysis system not only reduced the energy input but also produced formate with high Faradaic efficiency.

2. Materials and methods

2.1 Chemicals and materials

Cobalt (II) nitrate hexahydrate ($Co(NO_3)_2·6H_2O$, AR, 98%), potassium hydroxide (KOH, GR, 85%), iron (III) nitrate nonahydrate ($Fe(NO_3)_3·9H_2O$, AR, 98.5%), iron (III) chloride hexahydrate ($FeCl_3·6H_2O$, AR, 99%), sodium hydroxide (NaOH, AR, 96%), sodium carbonate (Na_2CO_3, AR, 99.8%), anhydrous methanol, anhydrous ethylene glycol, anhydrous ethanol, and N,N′-dimethylformamide (DMF) were purchased from Sinopharm Chemical Reagent Co. Ltd. (Shanghai, China). Potassium trioxalatoferrate (III) trihydrate ($K_3[Fe(C_2O_4)_3]$, 99%) was purchased from Macklin Biochemical Technology Co. Ltd. (Shanghai, China). Nafion solution (5 wt%) and 2-methylimidazole were bought from Aladdin Reagent. Carbon paper was bought from Shanghai He Sen Electric Co. Ltd. Deionized H_2O was used during all experiments.

2.2 Synthesis

2.2.1 Synthesis of ZIF-67 nanocrystals

Co-based MOF precursor (ZIF-67) was prepared via the solvothermal assembly of Co^{2+} and 2-methylimidazole ligand. Typically, 2.91 g of $Co(NO_3)_2·6H_2O$ and 3.28 g of

2-methylimidazole were each dissolved in 200 mL of methanol. Then, the solution of 2-methylimidazole was rapidly poured into the solution of $Co(NO_3)_2 \cdot 6H_2O$ under vigorous stirring. After reacting at room temperature for 24 h, the resulting purple precipitate was collected by centrifugation, washed 3 times with methanol, and vacuum-dried at 60°C overnight.

2.2.2 Synthesis of hollow h-CoFe-LDH NCs and yolk–shell ys-ZIF@CoFe-LDH NCs

Oxalate-modified hollow h-CoFe-LDHs NCs were synthesized by using the previously prepared ZIF-67 as the template. Typically, 100 mg of ZIF-67 was first ultrasonically dispersed in 20 mL of ethanol. Then 20 mL of $K_3[Fe(C_2O_4)_3]$ aqueous solution (1.5 mg mL^{-1}) was slowly added. The mixture was then refluxed at 85°C for 60 min. After cooling to room temperature, the product was collected by centrifugation, washed with ethanol 3 times, and dried at 60°C for 10 hours. To obtain the oxalate-modified yolk–shell ys-ZIF@CoFe-LDH NCs, the reaction was aged at room temperature for 30 min. Finally, the product was collected by centrifugation, washed with ethanol several times, and dried at 60°C overnight.

2.2.3 Synthesis of typical CoFe-LDH NSs

Typical CoFe-LDH nanosheets (t-CoFe-LDH NSs) were prepared as follows. 5.25 mmol of $Co(NO_3)_2 \cdot 6H_2O$ and 0.75 mmol of $Fe(NO_3)_3 \cdot 9H_2O$ were dissolved in 40 mL of deionized water to form solution A. 3 mmol of Na_2CO_3 and 21 mmol of NaOH were dissolved in 40 mL of deionized water to form solution B. Then, solutions A and B were simultaneously added dropwise into a beaker containing 80 mL of deionized water until the pH of the final solution reached 8.5. After 24 h of stirring, the precipitates were collected and dried at 60°C overnight.

2.2.4 Synthesis of hollow h-Co-LDH NCs

Hollow h-Co-LDH NCs were prepared similarly to h-CoFe-LDH NCs. Typically, 100 mg of ZIF-67 was dispersed in 25 mL of ethanol containing 180 mg of $Co(NO_3)_2·6H_2O$. Then the mixture was refluxed at 85°C for 60 min. Finally, the collected product was washed with ethanol several times and dried at 60°C overnight.

2.3 Physical characterizations

Powder X-ray diffraction (PXRD) patterns of the samples were collected on a Rigaku-Miniflex 600 diffractometer with Cu Kα radiation (step size = 0.02, scan rate = $2° \text{ min}^{-1}$). Scanning electron microscope (SEM) characterization was performed on a Carl Zeiss Sigma 300 microscope. Transmission electron microscopy (TEM) and high-resolution TEM (HRTEM) images of the samples were obtained using a Talos-F200X microscope. X-ray photoelectron spectroscopy (XPS) spectra were collected on an ESCALAB 250Xi with monochromatic Al Kα radiation (E = 1486.2 eV), and the binding energies were calibrated by the C 1s peak at 284.8 eV. Fourier transform infrared (FTIR) spectra were recorded on a FTIR spectrometer (Vertex70). Raman spectra were recorded using a LabRAM HR Raman microscope with a 532 nm laser. After treatment under vacuum at 120°C for 12 h, the N_2 sorption isotherms were measured using a BELSORP Max analyzer at liquid nitrogen temperature (77 K).

2.4 Electrochemical characterizations

OER and EGOR measurements were performed in a three-electrode cell connected to an electrochemical workstation (CHI 660E), where carbon rod and saturated Ag/AgCl electrode were used as the counter electrode and reference electrode, respectively. 1.0 M KOH with or without 0.5 M ethylene glycol was used as the electrolyte. The catalyst ink was prepared by dispersing 10 mg of catalyst in a mixture of H_2O (200 μL), EtOH (700 μL), DMF (50 μL), and Nafion solution (50 μL, 5 wt%), followed by ultrasonication for 1 h to form a homogeneous suspension. Then, 200 μL of the catalyst ink was deposited on a 1.0 × 1.0 cm^2 piece of carbon paper substrate to obtain a loading of 2 mg cm^{-2}. The linear sweep voltammetry (LSV) polarization curves were recorded at a scan rate of 5 mV s^{-1} with 90% *iR*-compensation. All measured potentials in this work were calibrated to the reversible hydrogen electrode (RHE): $E_{RHE} = E_{Ag/AgCl} + 0.059 \times pH + 0.197$ (V). The overpotential (η) of the OER was calculated according to the following formula: $\eta = E_{RHE} - 1.23$ V. Electrochemical impedance spectroscopy (EIS) spectra were recorded with the frequency ranging from 0.01 to 10^5 Hz at an AC amplitude of 5 mV.

2.5 Product analysis

The liquid products (formate) during the EGOR were quantified and analyzed by ^1H nuclear magnetic resonance (NMR) spectroscopy. In a typical analysis, a mixture of 0.5 mL of the electrolyte and 0.1 mL of 10 mM DMSO (as internal standard) D_2O solution was used as the measured sample. The ^1H NMR spectra were obtained by using a pre-saturation method to suppress the water peak. The chemical formula for the EGOR to produce formate is as follows: $C_2H_6O_2 + 8OH^- \rightarrow 2HCOO^- + 6H_2O + 6e^-$.

The FE of formate was calculated by the equation FE= nNF/Q, where n is the mole of product, N is 3 for formate of the EGOR, F is the Faradaic constant (96,485 C mol^{-1}), and Q is the total charge passed through the working electrode.

3. Results and discussion

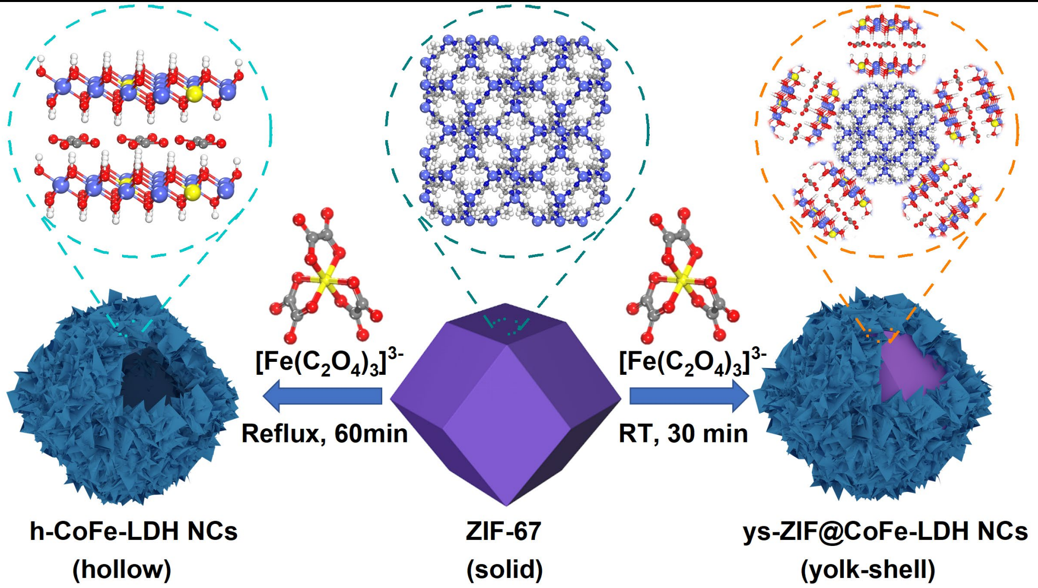

Fig. 1. Schematic illustration of the fabrication of h-CoFe-LDH NCs and ys-ZIF@CoFe-LDH NCs.

As shown in **Fig. 1**, hierarchical CoFe-LDH-based nanocages with two different nanostructures can be prepared by using an etching–doping reconstruction strategy, starting from Co-MOF (ZIF-67) precursor. ZIF-67 nanocrystals with a rhombic dodecahedral morphology were first synthesized as sacrificial templates via the assembly of Co^{2+} and 2-methylimidazole ligands under ambient conditions (**Fig. S1**). After the reaction between $K_3[Fe(C_2O_4)_3]$ and ZIF-67 in an ethanol–water solution, hollow h-CoFe-LDH NCs and yolk–shell ys-ZIF@CoFe-LDH NCs were obtained under refluxing and ambient conditions, respectively. We speculate that during the reconstruction process, the ZIF-67 template was gradually etched by the H^+ generated from the hydrolysis of $[Fe(C_2O_4)_3]^{3-}$; meanwhile, the released Fe^{3+} and Co^{2+} coprecipitated with $OH^-/C_2O_4^{2-}$ to form a thin CoFe-LDH NSs shell [14]. Since $K_3[Fe(C_2O_4)_3]$ is insoluble in ethanol, an ethanol–water solution with the correct ratio was essential for reconstructing ZIF-67. Moreover, the reconstruction degree could be readily controlled by adjusting the reaction temperature. Specifically, low temperature slowed down the etching of ZIF-67, leading to the formation of yolk–shell ys-

ZIF@CoFe-LDH NCs, whereas refluxing at high temperature led to faster hydrolysis and consequently hollow h-CoFe-LDH NCs.

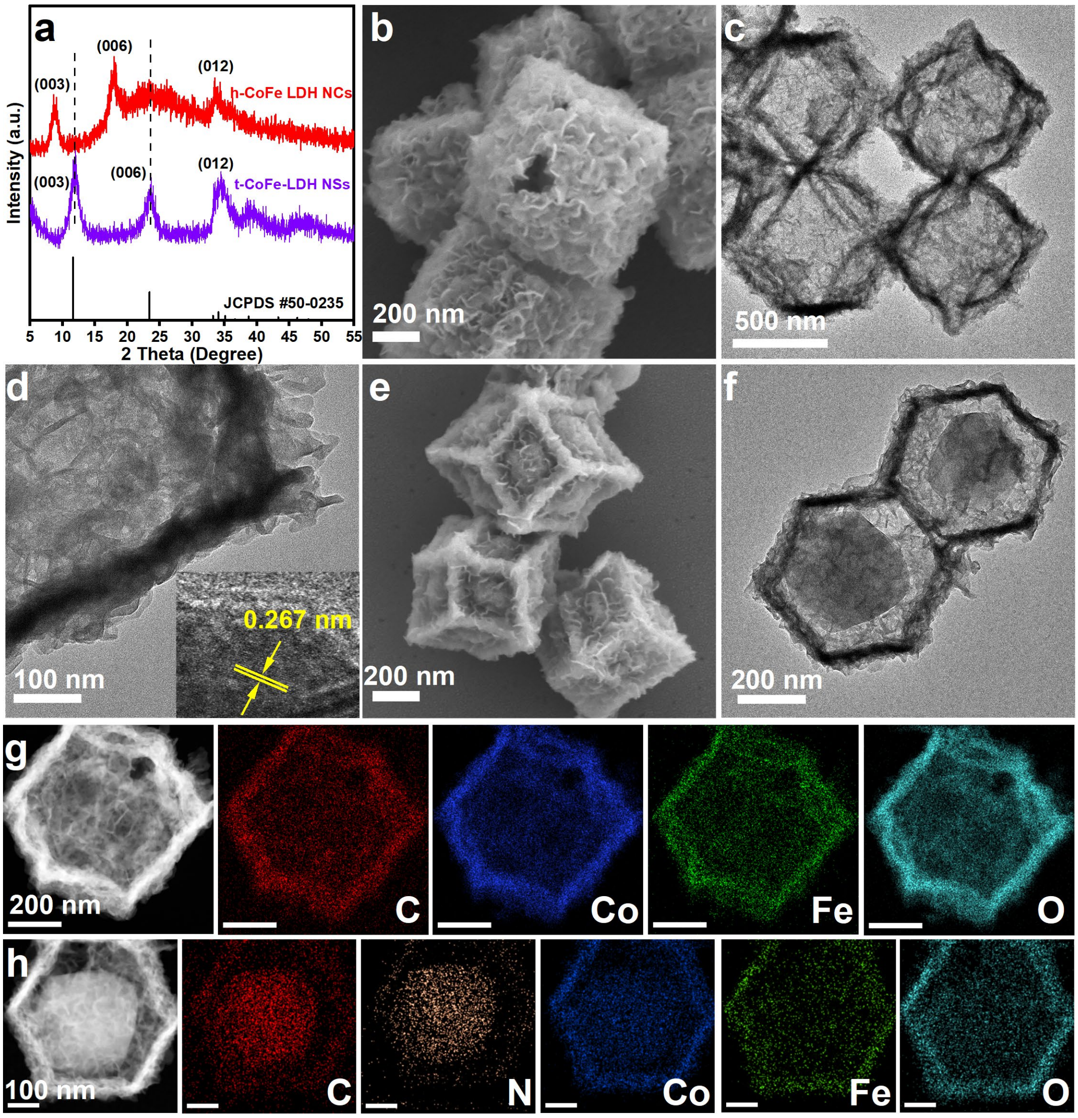

Fig. 2. (a) PXRD patterns of h-CoFe-LDH NCs and typical CoFe-LDH NSs (t-CoFe-LDH NSs); SEM and TEM images of (b–d) h-CoFe-LDH NCs and (e, f) ys-ZIF@CoFe-LDH NCs; HAADF-STEM and the corresponding EDX elemental mapping images of (g) h-CoFe-LDH NCs and (h) ys-ZIF@CoFe-LDH NCs.

For h-CoFe-LDH NCs, the diffraction peaks corresponding to ZIF-67 disappeared after reflux treatment (**Figs. 2a**). Instead, new diffraction peaks located at 8.8, 17.9, and 33.8° were observed, which can be assigned to the typical LDH phase (labelled as t-

CoFe-LDH NSs, JCPDS No. 50-0235) but with a certain shift, indicating a complete conversion of ZIF to the LDH phase (**Fig. S2**). Compared to t-CoFe-LDH NSs with CO_3^{2-} as the intercalated anions, the diffraction peaks of h-CoFe-LDH NCs indexed as (003) and (006) shifted to lower 2θ values. This was caused by the intercalation of larger $C_2O_4^{2-}$ anions, which led to interlayer expansion in the derived CoFe-LDH [34, 35]. In contrast, the PXRD pattern of the ys-ZIF@CoFe-LDH NCs was similar to that of pristine ZIF-67 but with weaker peak intensity (**Fig. S3**), implying that only part of the ZIF-67 was converted into CoFe-LDH, which has poor crystallinity. SEM and TEM images show that the as-prepared h-CoFe-LDH NCs inherited the dodecahedral morphology of ZIF-67 and displayed an ingenious hollow nanocage morphology, while the smooth surfaces of ZIF-67 turned into a rough shell composed of randomly oriented nanosheets (**Figs. 2b, c**). A lattice spacing of 0.267 nm in the HRTEM image can be indexed to the (012) plane of LDH (**Fig. 2d, inset**). SEM energy-dispersive X-ray (EDX) analysis indicated the presence of C, Fe, Co, and O in the h-CoFe-LDH NCs, with a Co:Fe atomic ratio of ~7.15 (**Fig. S4**), which is close to the value of 6.7 obtained from inductively coupled plasma optical emission spectrometry (ICP-OES) analysis. High-angle annular dark-field scanning TEM (HAADF-STEM) imaging and the corresponding elemental mapping images show a uniform distribution of C, Co, Fe, and O throughout the hollow nanocages (**Fig. 2g**). Comparatively, the ys-ZIF@CoFe-LDH NCs exhibited an intriguing yolk–shell structure consisting of a CoFe-LDH nanosheet-based shell ~40 nm in thickness and a maternal ZIF-67 core ~250 nm in diameter (**Figs. 2e, f**). The CoFe-LDH shells of the ys-ZIF@CoFe-LDH NCs were similar to those of the h-CoFe-LDH NCs. The representative EDX elemental mapping analysis confirmed that the inner core consisted of only C, N, and Co, while the outer shell contained primarily Co, Fe, and O (**Fig. 2h**), further verifying the CoFe-LDH shell and ZIF-67 core in the ys-ZIF@CoFe-LDH NCs. For comparison, t-CoFe-LDH NSs with the same Co:Fe ratio and hollow Co-LDH NCs (h-Co-LDH NCs) were also prepared (**Figs. S5–6**).

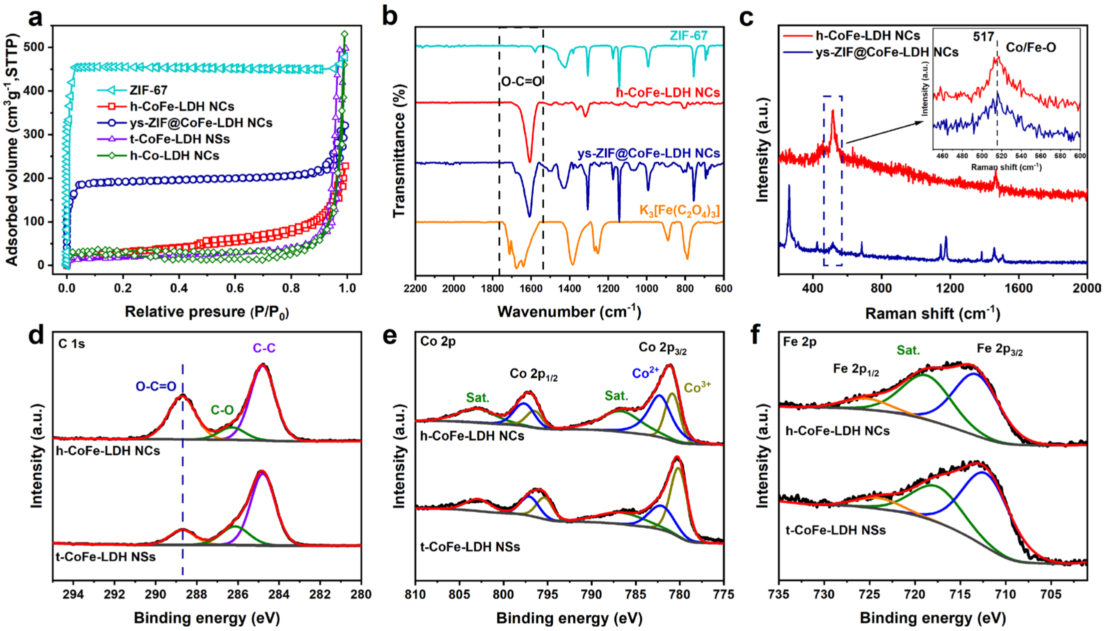

Fig. 3. (a) N_2 sorption isotherms of ZIF-67, h-CoFe-LDH NC, ys-ZIF@CoFe-LDH NCs, t-CoFe-LDH NSs, and h-Co-LDH NCs. (b) FTIR spectra of ZIF-67, h-CoFe-LDH NCs, ys-ZIF@CoFe-LDH NCs, and $K_3[Fe(C_2O_4)_3]$. (c) Raman spectra of h-CoFe-LDH NCs and ys-CoFe-LDH NCs. High-resolution XPS spectra of (d) C 1s, (e) Co 2p, and (f) Fe 2p for h-CoFe-LDH NCs and t-CoFe-LDH NSs.

The textural properties of h-CoFe-LDH NCs, ys-ZIF@CoFe-LDH NCs, t-CoFe-LDH NSs, and h-Co-LDH NCs were further analyzed by N_2 adsorption–desorption isotherms. As shown in **Fig. 3a**, the h-CoFe-LDH NCs and h-Co-LDH NCs displayed type-II isotherms with BET surface areas of 109 and 104 m^2 g^{-1}, respectively, higher than that of t-CoFe-LDH NSs (65 m^2 g^{-1}), indicating the formation of a hollow hierarchical structure with a higher surface area that provided more accessible active sites for electrochemical reaction. In contrast, the ys-ZIF@CoFe-LDH NCs showed a type-I isotherm similar to pristine ZIF-67, with a BET surface area of 759 m^2 g^{-1}, suggesting that part of the ZIF-67 was preserved.

To understand the formation of the nanocage morphology of h-CoFe-LDH NCs and ys-ZIF@CoFe-LDH NCs, the reconstruction-induced agent $K_3[Fe(C_2O_4)_3]$ was replaced by other Fe salts, such as $FeCl_3·6H_2O$ and $Fe(NO_3)_3·9H_2O$. In contrast, only polyhedral particles with smooth surfaces and cracked particles were obtained (**Fig. S7**), proving that the oxalate group was crucial for the formation of the distinctive morphologies in the h-CoFe-LDH NCs and ys-ZIF@CoFe-LDH NCs. According to coordination chemistry theory, the leached Co^{2+} was able to coordinate with $C_2O_4^{2-}$ to form a stable coordination complex around ZIF-67 particles during the etching process [36]. Hence, the strong affinity between the etchant and the ZIF-67 template enabled the fabrication of hierarchical nanocages [4]. In contrast, the coordination ability of Cl^- and NO_3^- was too weak to form an exterior hierarchical LDH shell that mimicked the ZIF-67 template geometry. The amount of $K_3[Fe(C_2O_4)_3]$ added was also important in determining the final morphology. As shown in **Fig. S8**, a very small amount of $K_3[Fe(C_2O_4)_3]$ could not induce the formation of hollow structures (**Figs. S8a, b**), while too much $K_3[Fe(C_2O_4)_3]$ led to over-etching of the ZIF-67 framework, causing the collapse of the polyhedra (**Figs. S8g, h**).

Analysis of the FTIR spectra showed that compared with pristine ZIF-67 and h-Co-LDH NCs (**Figs. 3b and S9**), a new strong band at around 1610 cm^{-1} was observed in the h-CoFe-LDH NCs and ys-ZIF@CoFe-LDH NCs, which is assigned to the asymmetric C=O stretching vibration [37], indicating that the oxalate groups were intercalated into the CoFe-LDH NSs. According to previous work, the presence of the hydrophilic oxalate group can enhance the adsorption of water molecules on the catalyst surface and modify the electron structure of active sites, thereby improving electrochemical performance [38]. Raman spectra were also collected to gain more information on the bonding and chemical structure. As shown in **Fig. 3c,** the h-CoFe-LDH NCs displayed two peaks at about 455 and 517 cm^{-1}, attributed to Co-OH and Co-O bonds, respectively [39]. In comparison with the h-Co-LDH NCs (**Fig. S10**), the peaks corresponding to Co-O bonds in the h-CoFe-LDH NCs and t-CoFe-LDH NSs were red-shifted, indicating the elongation of Co-O bonds, likely caused by the strong interaction between the Co and Fe sites [40].

The surface compositions and chemical states of the samples were further investigated by XPS. As shown in **Fig. S11**, the survey spectra of the h-CoFe-LDH NCs, ys-ZIF@CoFe-LDH NCs, and t-CoFe-LDH NSs revealed the existence of C, Co, Fe, and O, whereas Fe was not detected in the h-Co-LDH NCs. Notably, the signal of N in the ys-ZIF@CoFe-LDH NCs is ascribed to the existence of the 2-methylimidazole ligand in the ZIF-67 cores. As observed in **Fig. 3d**, the C 1s XPS spectrum of the h-CoFe-LDH NCs can be deconvoluted into three peaks at 284.8, 285.9, and 288.7 eV, indexed to C-C, C-O, and O-C=O bonds [41], respectively, indicating the presence of oxalate, which is consistent with the PXRD and FTIR results. In the Co 2p XPS spectra (**Fig. 3e**), the deconvoluted peaks at 780.7 and 782.2 eV are attributed to Co^{3+} and Co^{2+}, respectively [42]. In comparison with the h-Co-LDH NCs (**Fig. S12**), the peaks of Co 2p in the h-CoFe-LDH NCs and ys-ZIF@CoFe-LDH NCs had shifted to a higher energy, demonstrating interactions between Co and Fe sites, which is consistent with Raman spectra results. The Fe 2p XPS spectra of the samples can be deconvoluted into two broad peaks at 725.3 and 713.2 eV, assigned to Fe $2p_{1/2}$ and Fe $2p_{3/2}$ signals, respectively, confirming that the Fe species in the CoFe-LDH phase are mostly in the +3 oxidation state [24] (**Fig. 3f**).

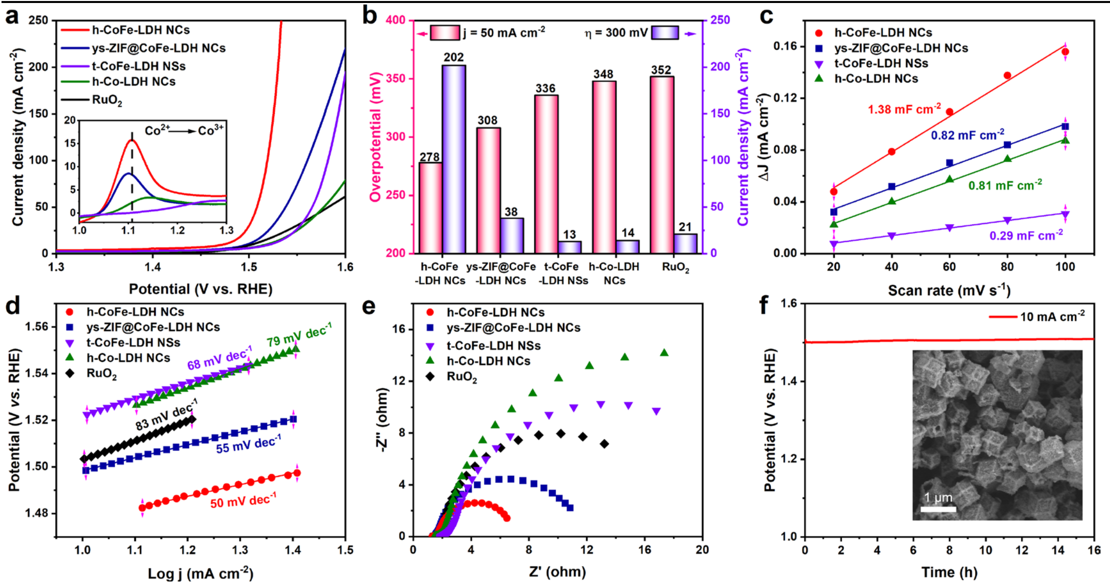

Fig. 4. OER performance of the catalysts: (a) LSV curves; (b) comparison of overpotential η at current density j = 50 mA cm^{-2}, and j at η = 300 mV; (c) capacitive Δj (= $j_a - j_c$) against scan rates; (d) Tafel plots; (e) EIS plots; (f) long-term stability test for h-CoFe-LDH NCs at j = 10 mA cm^{-2}. All the tests were conducted in 1.0 M KOH. Inset in (f) is a SEM image of h-CoFe-LDH NCs after the stability test.

The electrocatalytic OER performance of the as-prepared catalysts was investigated in 1.0 M KOH. Commercial RuO$_2$ was used as the reference. All electrocatalysts were loaded on a piece of carbon paper (CP) with a working area of 1.0 cm^2. As shown in **Fig. 4a**, ZIF-67-derived electrocatalysts displayed an oxidation peak of Co^{2+} to Co^{3+} at around 1.1 V. According to previous work, high-valence Co species (*i.e.*, Co^{3+}) are the active sites for the OER in Co-based electrocatalysts [43]. Based on the relationship between the anodic/cathodic current densities and the scan rates (**Figs. S13d–f**) [44], the surface coverage of the Co^{2+}/Co^{3+} redox couple was estimated to be 3.04 × 10^{-7} for the h-CoFe-LDH NCs, which was 1.05 and 2.09 times those of the ys-ZIF@CoFe-LDH NCs (2.90 × 10^{-7}) and h-Co-LDH NCs (1.45 × 10^{-7}), respectively. Moreover, the anodic and cathodic peak current densities for all the as-prepared catalysts were in proportion to the square root of the scan rates (**Figs. S13g–i**), suggesting that Co^{2+}/Co^{3+} redox is a proton diffusion-controlled process [45]. Notably, the calculated proton diffusion coefficient (*D*) value for the h-CoFe-LDH NCs (5.93×10^{-7}) was larger than for the ys-ZIF@CoFe-LDH NCs (5.37×10^{-7}) and h-Co-LDH NCs (1.21×10^{-7}) [46]. It is generally accepted that a larger *D* value induces a lower oxidation onset potential, which is beneficial for generating more Co^{3+} species. Consequently, the higher surface coverage of the Co^{2+}/Co^{3+} redox couple and faster proton diffusivity of the h-CoFe-LDH NCs should promote OER performance. This was indeed the case, as shown in **Figs. 4a, b and S14**, since the h-CoFe-LDH NCs required an overpotential (η) of only 278 mV to deliver a current density of 50 mA cm^{-2}; this was much lower than for the ys-ZIF@CoFe-LDH NCs (308 mV), t-CoFe-LDH NSs (336 mV), and h-Co-LDH NCs (348 mV), and even for commercial RuO_2 catalyst (352 mV), as well as many recently reported Co-based electrocatalysts (**Table S1**). More impressively, the h-CoFe-LDH NCs delivered a current density of about 202 mA cm^{-2} at $\eta = 300$ mV, which was much higher than the ys-ZIF@CoFe-LDH NCs (38 mA cm^{-2}), t-CoFe-LDH NSs (13 mA cm^{-2}), h-Co-LDH NCs (14 mA cm^{-2}), and RuO_2 (21 mA cm^{-2}), once again demonstrating its excellent OER activity.

To further investigate OER performance, the electrochemically active surface areas (ECSAs) of the as-prepared electrocatalysts, which are generally proportional to the double layer capacitances (C_{dl}), were measured based on CV curves at different scan rates (**Fig. S15**). As shown in **Fig. 4c**, the measured C_{dl} of the h-CoFe-LDH NCs was 1.38 mF cm^{-2}, while the values were only 0.82, 0.81, and 0.29 mF cm^{-2} for the ys-ZIF@CoFe-LDH NCs, t-CoFe-LDH NSs, and h-Co-LDH NCs, respectively. Moreover, the h-CoFe-LDH NCs also exhibited the highest current density normalized by ECSA among all the samples (**Fig. S16**). This outstanding performance is likely due to the synergistic effect arising from the distinctive micromorphology, the intercalation of oxalate species, and the bimetallic interactions.

The corresponding Tafel plots of the as-prepared electrocatalysts were then obtained to study the reaction kinetics. As shown in **Fig. 4d**, the h-CoFe-LDH NCs exhibited the smallest Tafel slope of 50 mV dec^{-1}, compared with the ys-ZIF@CoFe-LDH NCs (55 mV dec^{-1}), t-CoFe-LDH NSs (68 mV dec^{-1}), h-Co-LDH NCs (79 mV dec^{-1}), and RuO_2 (83 mV dec^{-1}), demonstrating the enhanced OER kinetics. EIS plots of the samples were collected to gain insight into the charge transfer resistance during the OER. As displayed in **Fig. 4e**, the h-CoFe-LDH NCs possessed the smallest charge-transfer resistance compared with the ys-ZIF@CoFe-LDH NCs, t-CoFe-LDH NSs, h-Co-LDH NCs, and RuO_2, which would enhance the charge transfer kinetics, thereby promoting the OER activity.

The h-CoFe-LDH NCs also displayed good stability during long-term electrolysis. The chronoamperometric curve shows that the potential experienced negligible change while maintaining 10 mA cm^{-2} for more than 16 h (**Fig. 4f**). Meanwhile, SEM (**Fig. 4f, inset**) and TEM images (**Fig. S17**) show that the morphology of the h-CoFe-LDH NCs remained the same after the long-term durability test. However, totally different PXRD patterns (**Fig. S18**) and Raman spectra (**Fig. S19**) demonstrate the structural reconstruction of the catalyst during the OER process. XPS measurement of the h-CoFe-LDH NCs after the stability test showed some predictable changes (**Fig. S20**); namely, the high-resolution XPS of O 1s suggested the formation of oxyhydroxide (MOOH, 535 eV) [47]. Based upon the Raman and XPS results, we believe that the CoFe-LDH phase transformed into metal oxyhydroxide, which has been widely accepted as the real active species for the OER [43, 48].

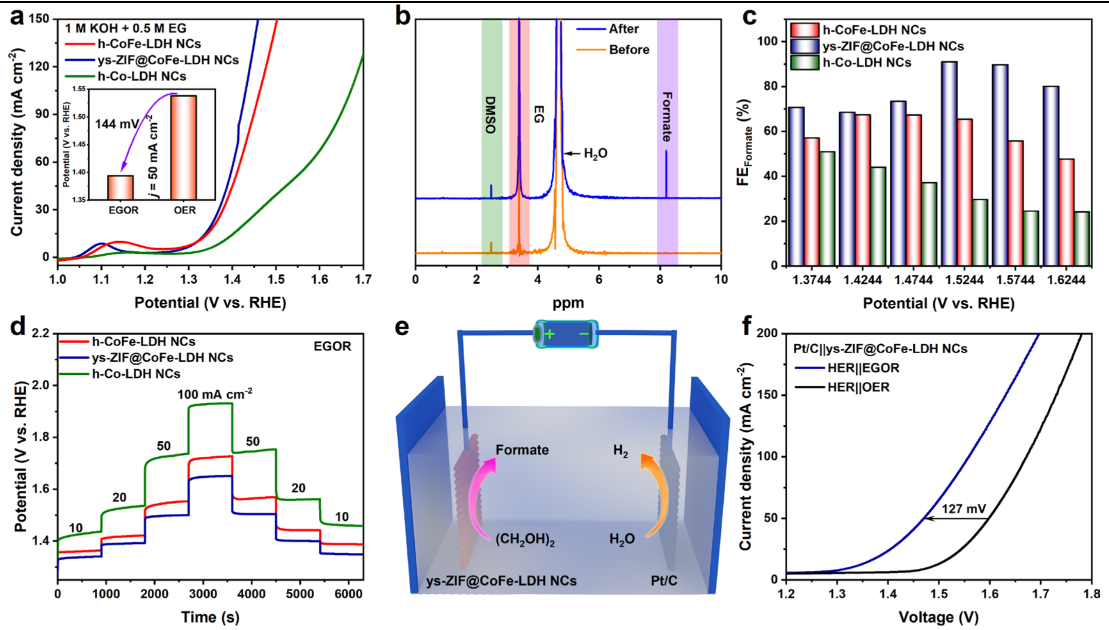

Fig. 5. (a–d) EGOR performance of the catalysts: (a) LSV curves; (b) ^{1}H NMR spectra of the electrolyte before and after electrolysis; (c) correlation between potential and FE$_{\text{formate}}$; (d) multi-step chronopotentiometry curves from 10 to 100 mA cm^{-2} without *iR*-compensation; (e) schematic illustration and (f) LSV curves of the HER||OER and HER||EGOR based on the Pt/C||ys-ZIF@CoFe-LDH NCs pair.

As mentioned above, replacing the OER with the thermodynamically favorable ethylene glycol (EG, a hydrolysate of polyethylene terephthalate (PET) plastic) oxidation reaction can simultaneously reduce energy input and upcycle PET plastic waste to produce value-added products. As a proof of concept, the electrocatalytic performance of the as-obtained catalysts toward the EGOR was also investigated. **Fig. 5a** shows that the h-CoFe-LDH NCs exhibited a much higher activity than the h-Co-LDH NCs. This is consistent with the literature identifying Co species (*e.g.*, Co^{3+}) as the real active species for the EGOR, whose activity can be further enhanced via moderate Fe doping [49]. Unlike for the OER, the ys-ZIF@CoFe-LDH NCs exhibited better EGOR activity than the h-CoFe-LDH NCs, possibly due to synergistic cooperation between the ZIF-67 cores and the CoFe-LDH shells. Specifically, the inner ZIF-67 core, with its high porosity and large surface area, could contribute to the enhanced absorption of EG molecules. The unique yolk–shell structure thus would enable EG enrichment within the voids during the electrocatalytic process and subsequently enhance the EGOR performance. Specifically, the ys-ZIF@CoFe-LDH NCs needed only 1.39 V to reach 50 mA cm^{-2}, which was 20 and 150 mV lower than for the h-CoFe-LDH NCs and h-Co-LDH NCs, respectively. The voltage was 144 mV lower than what was required to deliver the same current density for the OER (**Fig. 5a, inset**), demonstrating the potential of replacing the OER with the EGOR to reduce energy input for water electrolysis.

The oxidation products during the EGOR were quantitatively analyzed using ^{1}H nuclear magnetic resonance (NMR) spectroscopy. Notably, formate was the only detectable liquid product during constant potential electrolysis (**Figs. 5b and S21**). The ys-ZIF@CoFe-LDH NCs yielded the highest Faradaic efficiencies for formate generation ($FE_{formate}$) (**Fig. 5c**) at all applied potentials compared with the h-CoFe-LDH NCs and h-Co-LDH NCs. The maximum $FE_{formate}$ of the ys-ZIF@CoFe-LDH NCs was 91%, compared with only 67% and 51% for the h-CoFe-LDH NCs and h-Co-LDH NCs, respectively. The ys-ZIF@CoFe-LDH NCs also provided the highest formate partial current density ($j_{formate}$) compared with the other two samples (**Fig. S22**), further indicating its excellent EGOR performance. Moreover, the ys-ZIF@CoFe-LDH NCs showed excellent long-term stability toward the EGOR, with negligible potential changes during multi-step and constant chronopotentiometry measurements (**Figs. 5d and S23–24**). It is worth noting that the slight increase in potential was caused by the continuous consumption of ethylene glycol during the electrolysis process.

Encouraged by the excellent EGOR performance of the ys-ZIF@CoFe-LDH NCs, we assembled an HER||EGOR hybrid system to generate H_2 and formate simultaneously, with commercial Pt/C and ys-ZIF@CoFe-LDH NCs serving as the cathode and anode, respectively (**Fig. 5e**). As shown in **Fig. 5f**, a cell voltage of 1.47 V was needed to deliver a current density of 50 mA cm^{-2} for the HER and EGOR concurrently, which was 127 mV lower than for the HER||OER. Pt/C||ys-ZIF@CoFe-LDH NCs also exhibited better HER||EGOR performance than Pt/C||h-CoFe-LDH NCs, Pt/C||h-Co-LDH NCs, and even Pt/C||RuO_2 (**Figs. S25–26**). Notably, the HER||EGOR performance of Pt/C||ys-ZIF@CoFe-LDH NCs was better than for most of the recently reported transition metal-based electrocatalysts (**Table S2**). The produced formate was quantitatively analyzed. As shown in **Fig. S27**, despite similar Faradaic efficiencies for H_2 generation (FE_{H2}), the $FE_{formate}$ values over Pt/C||ys-ZIF@CoFe-LDH NCs were the highest among all the electrode pairs.

4. Conclusion

In summary, we developed a facile etching–reconstruction strategy to prepare hollow h-CoFe-LDH NCs and yolk-shell ys-ZIF@CoFe-LDH NCs by using ZIF-67 nanocrystals as the template. Oxalate anions are crucial for forming such a distinctive morphology, which not only exposes abundant accessible active sites with enhanced intrinsic activity, but also facilitates charge and mass transport, thereby promoting electrochemical performance. Specifically, h-CoFe-LDH NCs exhibited outstanding OER performance, with an overpotential of only 278 mV to achieve a current density of 50 mA cm^{-2}, superior to commercial RuO_2 catalyst and Co-based electrocatalysts reported to date. The ys-ZIF@CoFe-LDH NCs also selectively electro-oxidized ethylene glycol to formate with a Faradaic efficiency as high as 91%. Assembly of ys-ZIF@CoFe-LDH NCs and commercial Pt/C catalyst into a HER||EGOR hybrid electrolysis system enabled efficient simultaneous production of H_2 and formate with less energy input. Our work sheds light on the development of efficient MOF-derived catalysts for desirable electrochemical reactions.

Author contributions

Minghong Huang: experiments, analysis, and drafting manuscript; Changsheng Cao: writing and editing; Li Liu: experiments; Wenbo Wei: data analysis and visualization; Qi-Long Zhu and Zhenguo Huang: supervision, conceptualization, data analysis, review, and editing.

Competing financial interests

The authors declare no competing financial interests.

Acknowledgments

The authors are grateful for the financial support of the National Natural Science Foundation of China (21901246, 22105203 and 22205235) and the Natural Science Foundation of Fujian Province (2020J01116 and 2021J06033). Z. Huang acknowledges the support under the Australian Research Council's Discovery Projects funding scheme (DP220103458) and Future Fellowship (FT190100658).

References

[1] Y.P. Zhu, C. Guo, Y. Zheng, S.-Z. Qiao, Surface and interface engineering of noble-metal-free electrocatalysts for efficient energy conversion processes, Acc. Chem. Res. 50 (2017) 915-923.

[2] G. Prieto, H. Tüysüz, N. Duyckaerts, J. Knossalla, G.-H. Wang, F. Schüth, Hollow nano-and microstructures as catalysts, Chem. Rev. 116 (2016) 14056-14119.

[3] X. Wang, J. Feng, Y. Bai, Q. Zhang, Y. Yin, Synthesis, properties, and applications of hollow micro-/nanostructures, Chem. Rev. 116 (2016) 10983-11060.

[4] Z.-X. Cai, Z.-L. Wang, Y.-J. Xia, H. Lim, W. Zhou, A. Taniguchi, M. Ohtani, K. Kobiro, T. Fujita, Y. Yamauchi, Tailored catalytic nanoframes from metal–organic frameworks by anisotropic surface modification and etching for the hydrogen evolution reaction, Angew. Chem. Int. Ed. 60 (2021) 4747-4755.

[5] X. Wang, Z. Na, D. Yin, C. Wang, Y. Wu, G. Huang, L. Wang, Phytic acid-assisted formation of hierarchical porous CoP/C nanoboxes for enhanced lithium storage and hydrogen generation, ACS Nano 12 (2018) 12238-12246.

[6] C.-C. Hou, L. Zou, Q. Xu, A hydrangea-like superstructure of open carbon cages with hierarchical porosity and highly active metal sites, Adv. Mater. 31 (2019) 1904689.

[7] J. Nai, Y. Tian, X. Guan, L. Guo, Pearson's principle inspired generalized strategy for the fabrication of metal hydroxide and oxide nanocages, J. Am. Chem. Soc. 135 (2013) 16082-16091.

[8] Y. Liu, J. Goebl, Y. Yin, Templated synthesis of nanostructured materials, Chem. Soc. Rev. 42 (2013) 2610-2653.

[9] J. Nai, J. Zhang, X.W. Lou, Construction of single-crystalline prussian blue analog hollow nanostructures with tailorable topologies, Chem 4 (2018) 1967-1982.

[10] Z. Li, M. Song, W. Zhu, W. Zhuang, X. Du, L. Tian, MOF-derived hollow heterostructures for advanced electrocatalysis, Coord. Chem. Rev. 439 (2021) 213946.

[11] L. Feng, K.-Y. Wang, G.S. Day, M.R. Ryder, H.-C. Zhou, Destruction of metal–organic frameworks: Positive and negative aspects of stability and lability, Chem. Rev. 120 (2020) 13087-13133.

[12] X. Li, Q.-L. Zhu, MOF-based materials for photo-and electrocatalytic CO_2 reduction, EnergyChem 2 (2020) 100033.

[13] W. Wang, H. Yan, U. Anand, U. Mirsaidov, Visualizing the conversion of metal–organic framework nanoparticles into hollow layered double hydroxide nanocages, J. Am. Chem. Soc. 143 (2021) 1854-1862.

[14] Z. Jiang, Z. Li, Z. Qin, H. Sun, X. Jiao, D. Chen, LDH nanocages synthesized with MOF templates and their high performance as supercapacitors, Nanoscale 5 (2013) 11770-11775.

[15] Y. Shi, B. Zhu, X. Guo, W. Li, W. Ma, X. Wu, H. Pang, MOF-derived metal sulfides for electrochemical energy applications, Energy Storage Mater. 51 (2022) 840-872.

[16] Y.-C. Zhang, C. Han, J. Gao, L. Pan, J. Wu, X.-D. Zhu, J.-J. Zou, NiCo-based electrocatalysts for the alkaline oxygen evolution reaction: a review, ACS Catal. 11 (2021) 12485-12509.

[17] J. Wang, W. Cui, Q. Liu, Z. Xing, A.M. Asiri, X. Sun, Recent progress in cobalt-based heterogeneous catalysts for electrochemical water splitting, Adv. Mater. 28 (2016) 215-230.

[18] F. Dionigi, Z. Zeng, I. Sinev, T. Merzdorf, S. Deshpande, M.B. Lopez, S. Kunze, I. Zegkinoglou, H. Sarodnik, D. Fan, A. Bergmann, J. Drnec, J.F.d. Araujo, M. Gliech,

D. Teschner, J. Zhu, W.-X. Li, J. Greeley, B.R. Cuenya, P. Strasser, In-situ structure and catalytic mechanism of NiFe and CoFe layered double hydroxides during oxygen evolution, Nat. Commun. 11 (2020) 2522.

[19] Z.-F. Huang, J. Song, K. Li, M. Tahir, Y.-T. Wang, L. Pan, L. Wang, X. Zhang, J.-J. Zou, Hollow cobalt-based bimetallic sulfide polyhedra for efficient all-pH-value electrochemical and photocatalytic hydrogen evolution, J. Am. Chem. Soc. 138 (2016) 1359-1365.

[20] Y. Huang, S.L. Zhang, X.F. Lu, Z.-P. Wu, D. Luan, X.W. Lou, Trimetallic spinel $NiCo_{2-x}Fe_xO_4$ nanoboxes for highly efficient electrocatalytic oxygen evolution, Angew. Chem. Int. Ed. 60 (2021) 11841-11846.

[21] B. Qiu, L. Cai, Y. Wang, Z. Lin, Y. Zuo, M. Wang, Y. Chai, Fabrication of nickel–cobalt bimetal phosphide nanocages for enhanced oxygen evolution catalysis, Adv. Funct. Mater. 28 (2018) 1706008.

[22] J. Shan, C. Ye, S. Chen, T. Sun, Y. Jiao, L. Liu, C. Zhu, L. Song, Y. Han, M. Jaroniec, Y. Zhu, Y. Zheng, S.-Z. Qiao, Short-range ordered iridium single atoms integrated into cobalt oxide spinel structure for highly efficient electrocatalytic water oxidation, J. Am. Chem. Soc. 143 (2021) 5201-5211.

[23] Z.-F. Huang, J. Song, Y. Du, S. Xi, S. Dou, J.M.V. Nsanzimana, C. Wang, Z.J. Xu, X. Wang, Chemical and structural origin of lattice oxygen oxidation in Co–Zn oxyhydroxide oxygen evolution electrocatalysts, Nat. Energy 4 (2019) 329-338.

[24] J. Zhang, L. Yu, Y. Chen, X.F. Lu, S. Gao, X.W. Lou, Designed formation of double-shelled Ni–Fe layered-double-hydroxide nanocages for efficient oxygen evolution reaction, Adv. Mater. 32 (2020) 1906432.

[25] J. Song, C. Wei, Z.-F. Huang, C. Liu, L. Zeng, X. Wang, Z.J. Xu, A review on fundamentals for designing oxygen evolution electrocatalysts, Chem. Soc. Rev. 49 (2020) 2196-2214.

[26] Z.W. Seh, J. Kibsgaard, C.F. Dickens, I. Chorkendorff, J.K. Nørskov, T.F. Jaramillo, Combining theory and experiment in electrocatalysis: Insights into materials design, Science 355 (2017) eaad4998.

[27] J.J. Tian, C.S. Cao, D.D. Ma, S.G. Han, Y.C. He, X.T. Wu, Q.L. Zhu, Killing two birds with one stone: selective oxidation of small organic molecule as anodic reaction to boost CO_2 Electrolysis, Small Struct. 3 (2022) 2100134.

[28] C. Cao, D.D. Ma, J. Jia, Q. Xu, X.T. Wu, Q.L. Zhu, Divergent paths, same goal: a pair-electrosynthesis tactic for cost-efficient and exclusive formate production by metal–organic-framework-derived 2D electrocatalysts, Adv. Mater. 33 (2021) 2008631.

[29] B. Zhu, Z. Liang, R. Zou, Designing advanced catalysts for energy conversion based on urea oxidation reaction, Small 16 (2020) 1906133.

[30] J.N. Hausmann, P.V. Menezes, G. Vijaykumar, K. Laun, T. Diemant, I. Zebger, T. Jacob, M. Driess, P.W. Menezes, In-liquid plasma modified nickel foam: NiOOH/NiFeOOH active site multiplication for electrocatalytic alcohol, aldehyde, and water oxidation, Adv. Energy Mater. 12 (2022) 2202098.

[31] S.G. Han, M. Zhang, Z.H. Fu, L. Zheng, D.D. Ma, X.T. Wu, Q.L. Zhu, Enzyme-inspired microenvironment engineering of a single-molecular heterojunction for promoting concerted electrochemical CO_2 reduction, Adv. Mater. 34 (2022) 2202830.

[32] L. Jiao, W. Wei, X. Li, C.-B. Hong, S.-G. Han, M.I. Khan, Q.-L. Zhu, Value-added formate production from selective ethylene glycol oxidation based on cost-effective self-supported MOF nanosheet arrays, Rare Met. 41 (2022) 3654-3661.

[33] K. Xiang, D. Wu, X. Deng, M. Li, S. Chen, P. Hao, X. Guo, J.L. Luo, X.Z. Fu, Boosting H_2 generation coupled with selective oxidation of methanol into value-added chemical over cobalt hydroxide@hydroxysulfide nanosheets electrocatalysts, Adv. Funct. Mater. 30 (2020) 1909610.

[34] X. Long, J. Li, S. Xiao, K. Yan, Z. Wang, H. Chen, S. Yang, A strongly coupled graphene and FeNi double hydroxide hybrid as an excellent electrocatalyst for the oxygen evolution reaction, Angew. Chem. Int. Ed. 53 (2014) 7584-7588.

[35] L. Zhang, J. Liang, L. Yue, K. Dong, J. Li, D. Zhao, Z. Li, S. Sun, Y. Luo, Q. Liu, Benzoate anions-intercalated NiFe-layered double hydroxide nanosheet array with enhanced stability for electrochemical seawater oxidation, Nano Research Energy 1 (2022) e9120028.

[36] L. Ren, P. Wang, Y. Han, C. Hu, B. Wei, Synthesis of $CoC_2O_4{\cdot}2H_2O$ nanorods and their thermal decomposition to Co_3O_4 nanoparticles, Chem. Phys. Lett. 476 (2009) 78-83.

[37] D.M. Mangiante, R.D. Schaller, P. Zarzycki, J.F. Banfield, B. Gilbert, Mechanism of ferric oxalate photolysis, ACS Earth Space Chem. 1 (2017) 270-276.

[38] C.-F. Li, J.-W. Zhao, L.-J. Xie, J.-Q. Wu, Q. Ren, Y. Wang, G.-R. Li, Surface-adsorbed carboxylate ligands on layered double hydroxides/metal–organic frameworks promote the electrocatalytic oxygen evolution reaction, Angew. Chem. Int. Ed. 60 (2021) 18129-18137.

[39] Z. Li, X. Zhang, Y. Kang, C.C. Yu, Y. Wen, M. Hu, D. Meng, W. Song, Y. Yang, Interface engineering of Co-LDH@MOF heterojunction in highly stable and efficient oxygen evolution reaction, Adv. Sci. 8 (2021) 2002631.

[40] S. Lee, L. Bai, X. Hu, Deciphering iron-dependent activity in oxygen evolution catalyzed by nickel–iron layered double hydroxide, Angew. Chem. Int. Ed. 59 (2020) 8072-8077.

[41] J. Xiao, S. Yang, Bio-inspired synthesis of NaCl-type $Co_xNi_{1-x}O$ ($0\leq x< 1$) nanorods on reduced graphene oxide sheets and screening for asymmetric electrochemical capacitors, J. Mater. Chem. 22 (2012) 12253-12262.

[42] Z. Zhao, H. Wu, H. He, X. Xu, Y. Jin, A high-performance binary Ni–Co hydroxide-based water oxidation electrode with three-dimensional coaxial nanotube array structure, Adv. Funct. Mater. 24 (2014) 4698-4705.

[43] M.S. Burke, M.G. Kast, L. Trotochaud, A.M. Smith, S.W. Boettcher, Cobalt–iron (oxy) hydroxide oxygen evolution electrocatalysts: the role of structure and composition on activity, stability, and mechanism, J. Am. Chem. Soc. 137 (2015) 3638-3648.

[44] X. Cui, W. Guo, M. Zhou, Y. Yang, Y. Li, P. Xiao, Y. Zhang, X. Zhang, Promoting effect of Co in Ni_mCo_n (m+n=4) bimetallic electrocatalysts for methanol oxidation reaction, ACS Appl. Mater. Interfaces 7 (2015) 493-503.

[45] J. Jia, L. Zhao, Y. Chang, M. Jia, Z. Wen, Understanding the growth of NiSe nanoparticles on reduced graphene oxide as efficient electrocatalysts for methanol oxidation reaction, Ceram. Int. 46 (2020) 10023-10028.

[46] A.A. Dubale, Y. Zheng, H. Wang, R. Hübner, Y. Li, J. Yang, J. Zhang, N.K. Sethi, L. He, Z. Zheng, W. Liu, High-Performance bismuth-doped nickel aerogel electrocatalyst for the methanol oxidation reaction, Angew. Chem. Int. Ed. 59 (2020) 13891-13899.

[47] P. Li, M. Wang, X. Duan, L. Zheng, X. Cheng, Y. Zhang, Y. Kuang, Y. Li, Q. Ma, Z. Feng, W. Liu, X. Sun, Boosting oxygen evolution of single-atomic ruthenium through electronic coupling with cobalt-iron layered double hydroxides, Nat. Commun. 10 (2019) 1711.

[48] L.J. Enman, M.B. Stevens, M.H. Dahan, M.R. Nellist, M.C. Toroker, S.W. Boettcher, Operando X-ray absorption spectroscopy shows iron oxidation is concurrent with oxygen evolution in cobalt–iron (oxy)hydroxide electrocatalysts, Angew. Chem. Int. Ed. 57 (2018) 12840-12844.

[49] F. Meng, C. Dai, Z. Liu, S. Luo, J. Ge, Y. Duan, G. Chen, C. Wei, R.R. Chen, J. Wang, Methanol electro-oxidation to formate on iron-substituted lanthanum cobaltite perovskite oxides, eScience 2 (2022) 87-94.